Volume 15
Number 21
7 November 2025
Pages 6243–6570

Catalysis Science & Technology

rsc.li/catalysis

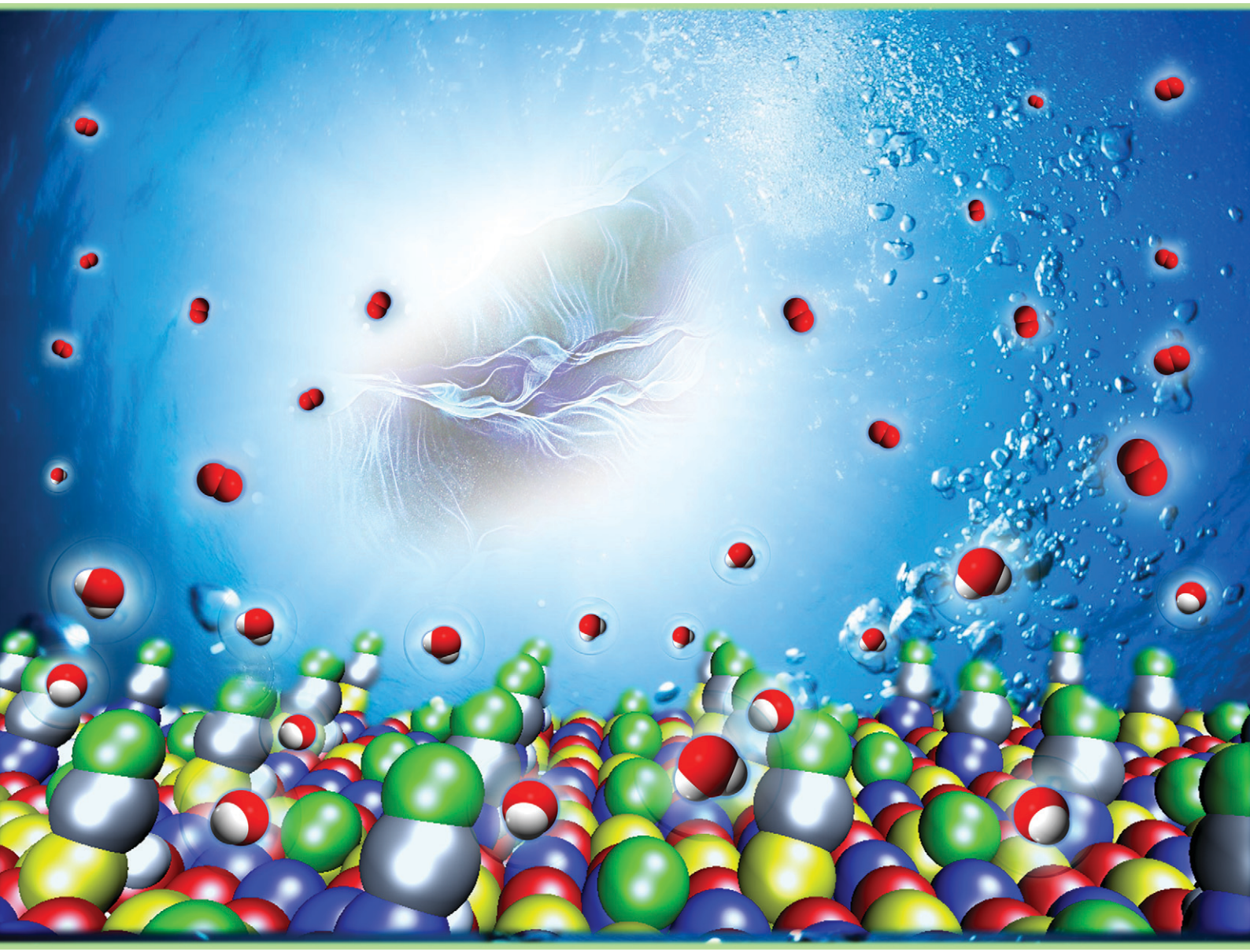

ISSN 2044-4761

ROYAL SOCIETY OF CHEMISTRY

PAPER

Chiara Maccato, Davide Barreca *et al.*
Plasma-assisted fabrication of NiO nanoarchitectures: from design to oxygen evolution electrocatalysis

Catalysis Science & Technology

ROYAL SOCIETY OF CHEMISTRY

PAPER

View Article Online
View Journal | View Issue

Cite this: *Catal. Sci. Technol.*, 2025, 15, 6358

Plasma-assisted fabrication of NiO nanoarchitectures: from design to oxygen evolution electrocatalysis

Chiara Maccato, *[ab] Davide Barreca, *[b] Lorenzo Signorin,[a] Enrico Scattolin,[a] Gloria Tabacchi,[c] Ettore Fois,[c] Cinzia Sada,[d] Oleg I. Lebedev,[e] Alberto Gasparotto,[ab] Evgeny Modin,[f] Ermanno Pierobon,[a] Naida El Habra[g] and Gian Andrea Rizzi[ab]

Electrocatalytic oxygen evolution reaction (OER), playing a key role in water splitting processes to yield green hydrogen, is critically dependent on the implementation of stable, efficient, and economically viable catalysts. Among the various runners, NiO-based nanomaterials have recently gained considerable attention. Herein, we focus on the plasma enhanced-chemical vapor deposition (PE-CVD) of NiO nanoarchitectures, grown on conducting glasses from a fluorinated Ni(II) precursor and subjected to a comprehensive experimental and theoretical characterization. Modulations of the growth temperature from 100 to 400 °C yielded a progressive evolution from hierarchical quasi-1D nanopillars, featuring the surface presence of CF_x groups, to cauliflower-like structures, characterized by a homogeneous fluorine distribution inside NiO. The open morphology of the 100 °C-grown system, possessing a higher content of structural defects, enhanced charge carrier transport and promoted reactants/products diffusion, yielding the best activity among the investigated materials (overpotential of ≈390 mV at 10 mA × cm^{-2} and Tafel slope of 39 mV × dec^{-1}). Density functional theory (DFT) modeling indicates that CF_x groups create intra-gap empty states which could promote OER activity. The obtained performances compare favorably with various Ni-based electrocatalysts reported up to date, opening the door to additional research developments towards sustainable energy generation.

Received 9th July 2025,
Accepted 18th September 2025

DOI: 10.1039/d5cy00833f

rsc.li/catalysis

Introduction

The ever-rising global energy demand, predicted to be to more than double by 2050,[1] can no longer be satisfied by the sole exploitation of fossil fuels, resulting in numerous environmental and health issues.[2–6] In this context, water electrolysis to yield green hydrogen has emerged as a clean and sustainable route to decarbonize the current energy portfolio.[7–15] Nevertheless, its large-scale utilization is hampered by the sluggish kinetics of the anodic oxygen evolution reaction (OER), hindering the achievement of technologically viable efficiencies.[5,16–22] To overcome this challenge, the development of efficient, stable and cost-effective OER electrocatalysts is a mandatory task.[10–12,23] Nickel(II) oxide, endowed with good stability and low cost, has a remarkable potential as precious metal-free electrocatalyst for alkaline OER.[3,20,24–26] As a result, different strategies have been explored to develop NiO-based nanostructures,[4,23,27–29] whose characteristics can be modulated according to the synthesis route and processing conditions.[30,31] In various cases, powdered catalysts are processed into a slurry/ink and applied on conductive substrates using a binder,[6,9,21,32] but unfortunately these systems are affected by modest conductivity, particle aggregation and low stability. These limitations can be addressed by the direct growth of the target materials onto suitable substrates.[2,7,18,24]

Over the last years, we have reported on the vapor phase synthesis of first-row transition metal oxide films/nanostructures from fluorinated diketonate-diamine molecular precursors [M(β-dik)$_2$TMEDA, with M = Mn,[33–37] Fe,[38–40] Co;[18,41,42] β-dik = tfa (1,1,1-trifluoro-2,4-pentanedionate) or hfa (1,1,1,5,5,5-hexafluoro-2,4-pentanedionate),

[a] Department of Chemical Sciences, Padova University and INSTM, 35131 Padova, Italy. E-mail: chiara.maccato@unipd.it
[b] CNR-ICMATE and INSTM, Department of Chemical Sciences, Padova University, 35131 Padova, Italy. E-mail: davide.barreca@unipd.it
[c] Department of Science and High Technology, Insubria University and INSTM, 22100 Como, Italy
[d] Department of Physics and Astronomy, Padova University and INSTM, 35131 Padova, Italy
[e] Laboratoire CRISMAT, UMR 6508 CNRS/ENSICAEN/UCBN, 14050 Caen Cedex 4, France
[f] CIC nanoGUNE BRTA, 20018 Donostia, San Sebastian, Spain
[g] CNR-ICMATE, 35127 Padova, Italy

and TMEDA = *N*,*N*,*N*′,*N*′-tetramethylethylenediamine]. The results demonstrated that, under suitable conditions, these compounds act as single-source molecular precursors for both M and F, yielding materials with a tunable fluorine content. For electrocatalytic applications, low temperature plasma technology[43] and, in particular, plasma enhanced-chemical vapor deposition (PE-CVD), are efficient and flexible fabrication methods,[5] thanks to the possibility of yielding nanosystems with unique properties under non-equilibrium conditions. Up to date, only a few works have been dedicated to the PE-CVD of nickel(II) oxide materials.[44–46]

Basing on preliminary results,[31] we report herein on the PE-CVD of NiO nanomaterials on fluorine-doped tin oxide (FTO) glass substrates from Ni(tfa)$_2$TMEDA, already used as a precursor in the thermal CVD of nickel(II) oxide.[47] The present materials, grown at different temperatures (Fig. 1), were subjected to a thorough characterization, supported by density functional theory (DFT)-based calculations. Interestingly, this approach enabled the simultaneous control of material morphology, chemical composition, microstrain, and dislocation density. Indeed, the last two parameters are pivotal in tailoring the properties of nanostructured systems[48] and, in particular, the molecular interactions between reactants and catalytic surfaces, enhancing thus the ultimate OER activity.[49] The best performances, well positioned in the panorama of NiO-based OER electrocatalysts, were obtained for the systems grown at 100 °C, the lowest ever reported up to date in the PE-CVD of nickel(II) oxide.[44–46] In perspective, the outcomes of the present study can be beneficial for the design of efficient and low-cost catalyst systems based on transition metal oxides.

Results and discussion

Material characterization

X-ray diffraction (XRD) patterns of the target specimens (Fig. 2a) evidenced, beside FTO substrate reflections, peaks located at 2θ = 37.3°, 43.3°, and 62.9°, attributed respectively to the (111), (200), and (220) crystallographic planes of cubic NiO (space group: $Fm\bar{3}m$).[50] Consistently with the face-centered cubic (fcc) nickel(II) oxide lattice, the observed reflections obeyed selection rules with Miller indexes (*hkl*) being either all even, or all odd.[47] Relative peak intensities were found to depend on the adopted growth temperature (see also the SI, S3). The average crystallite sizes underwent a progressive increase at higher substrate temperatures, *i.e.* upon enhancing the thermal energy supply (Fig. 2a, inset),[51] similarly to the case of MnO_2 nanosystems obtained *via* PE-CVD starting from an analogous molecular precursor.[37] The microstrain (ε) and dislocation density (δ) values [calculated using eqn. (S2) and (S3), SI] are plotted in Fig. 2b and c. In general, δ and ε values are directly dependent not only on material fabrication route, but also on the processing conditions.[47] In the present case, δ and ε values decreased for higher crystallite dimensions, in line with previous studies.[47,51,52] Dislocation density values were compatible with those reported for NiO films obtained by sputtering on Si(100) and glass substrates.[51–53] Altogether, these results indicated that a lower growth temperature is correlated to a larger content of structural defects.[37] As discussed below, the highest microstrain and dislocation density values obtained for the specimens grown at 100 and 200 °C directly contribute to the enhanced functional performances of these catalysts in comparison to the 300 °C and 400 °C-grown samples.

The system chemical composition was investigated by X-ray photoelectron spectroscopy (XPS), that yielded qualitatively similar results regardless of the adopted growth temperature. Wide-scan spectra (Fig. 3a) displayed the presence of C (see the related comments in the SI, as well as Fig. S3 and Table S1), O, Ni, and F photopeaks. A weak Sn 3d signal (corresponding to ≈0.2 at% of tin) was present only for the specimen grown at 100 °C, in accordance with the corresponding material morphology (see below and Fig. 6). For all the target samples, Ni 2p photoelectron peaks (Fig. 3b and S4 in the SI) presented very similar shapes and energy positions, and were characterized by the absence of features at a binding energy (BE) of 852.5 eV, ruling out the occurrence of metallic Ni.[10,28,54] Differently from a simple spin-orbit doublet, these peaks appeared as complex signals characterized by the presence of intense satellites at BEs ≈6 eV higher than the main spin-orbit components. The actual Ni 2p lineshape, directly influenced by multi-electron interactions between the emitting metal center and its nearest neighbors, was typical for the presence of Ni(II) in NiO.[2,6,14,32,47,55] The signal could be fitted by means of contributing bands positioned at 853.6 eV, 855.6 eV, 860.5 eV, 862.8 eV, 865.9 eV (j = 3/2), and 871.3 eV, 873.4 eV, 877.1 eV, 880.1 eV, and 883.2 eV (j = 1/2), for whose interpretation the reader is referred to previous

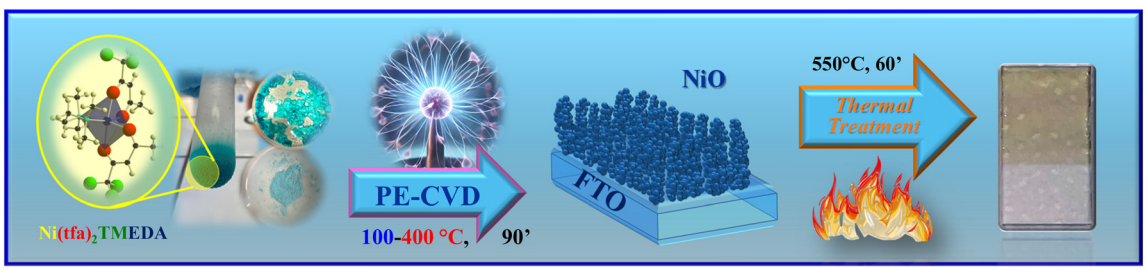

Fig. 1 Schematic representation of the route adopted in the present work for the synthesis of NiO electrocatalysts on FTO substrates.

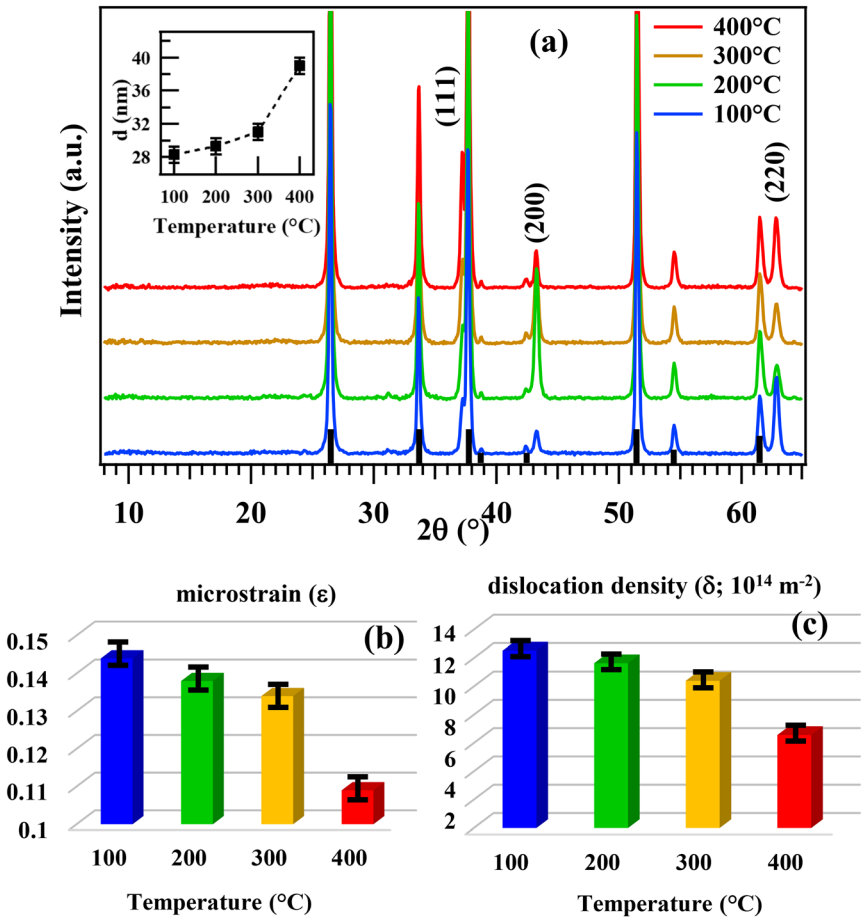

Fig. 2 (a) XRD patterns of NiO specimens obtained at different growth temperatures. Curves have been vertically shifted for clarity. Reflections of the FTO substrate are marked by vertical black bars. Inset: average crystallite dimensions [estimated using eqn. (S1) in the SI] as a function of growth temperature. Microstrain (b) and dislocation density values (c) for the same specimens.

works.[16,55] At variance with other studies,[22] no net evidence of Ni(III) occurrence was obtained from spectral analysis.

The O 1s photoelectron peaks (Fig. 3c and S5 in the SI) were deconvoluted by two different components, located at 529.8 eV (I) and 531.5 eV (II). The predominant one (I) was ascribed to lattice oxygen in NiO,[12,23,31,47] whereas band (II) resulted from the concomitant contribution of hydroxyl and carbonate groups chemisorbed on O defects.[21,31,35,47,55,56] A detailed analysis of fitting results (Table S2, SI) revealed a slight increase of band (II) contribution to the overall O 1s signal at expenses of component (I) upon increasing the growth temperature. In parallel, the O/Ni at% ratio underwent a modest decrease from (0.97 ± 0.02) to (0.89 ± 0.02) upon going from the 100 °C to the 400 °C specimen, suggesting thus the formation of NiO featuring a moderate oxygen deficiency.

Recently, oxygen vacancies engineering was applied to boost the OER activities of NiO electrocatalysts *via* the optimization of the system characteristics.[17,28,57] Nevertheless, in the present case the occurring variations are very modest, and cannot significantly contribute to the observed reactivity trend.

The F 1s peak features (Fig. 3d and S6 in the SI) were directly dependent on the adopted deposition temperature. For $T \geq 200$ °C, the F 1s signal was characterized by two components, positioned at mean BE = 684.5 eV (III) and 688.2 eV (IV) (Table S3, SI). The former, associated to Ni–F bonds, revealed a successful fluorine incorporation into NiO lattice, yielding thus F-doped NiO nanomaterials,[36,58,59] a result enabled by the used fluorinated precursor. Component (IV), ascribed to precursor-derived CF_x groups,[31,36,42] underwent a progressive decrease at higher growth temperatures (see Fig. 3e, pink curve, and S6, SI). At 100 °C, component (IV) was the only one contributing to the F 1s signal. These trends, displayed in Fig. 3e, underscore the possibility of modulating the nature and content of F-containing moieties in the target NiO nanosystems, enabling a parallel tailoring of OER functional activity (see below).

Additional information on the in-depth composition was obtained by secondary ion mass spectrometry (SIMS; Fig. 4). The average C content in the samples was estimated to be as low as tenths of ppm, suggesting thus a clean conversion of the used precursor into NiO under the adopted conditions. In fact, the ionic yields of nickel and oxygen evidenced an even composition throughout the investigated thickness, irrespective of the adopted growth temperature. The obtained

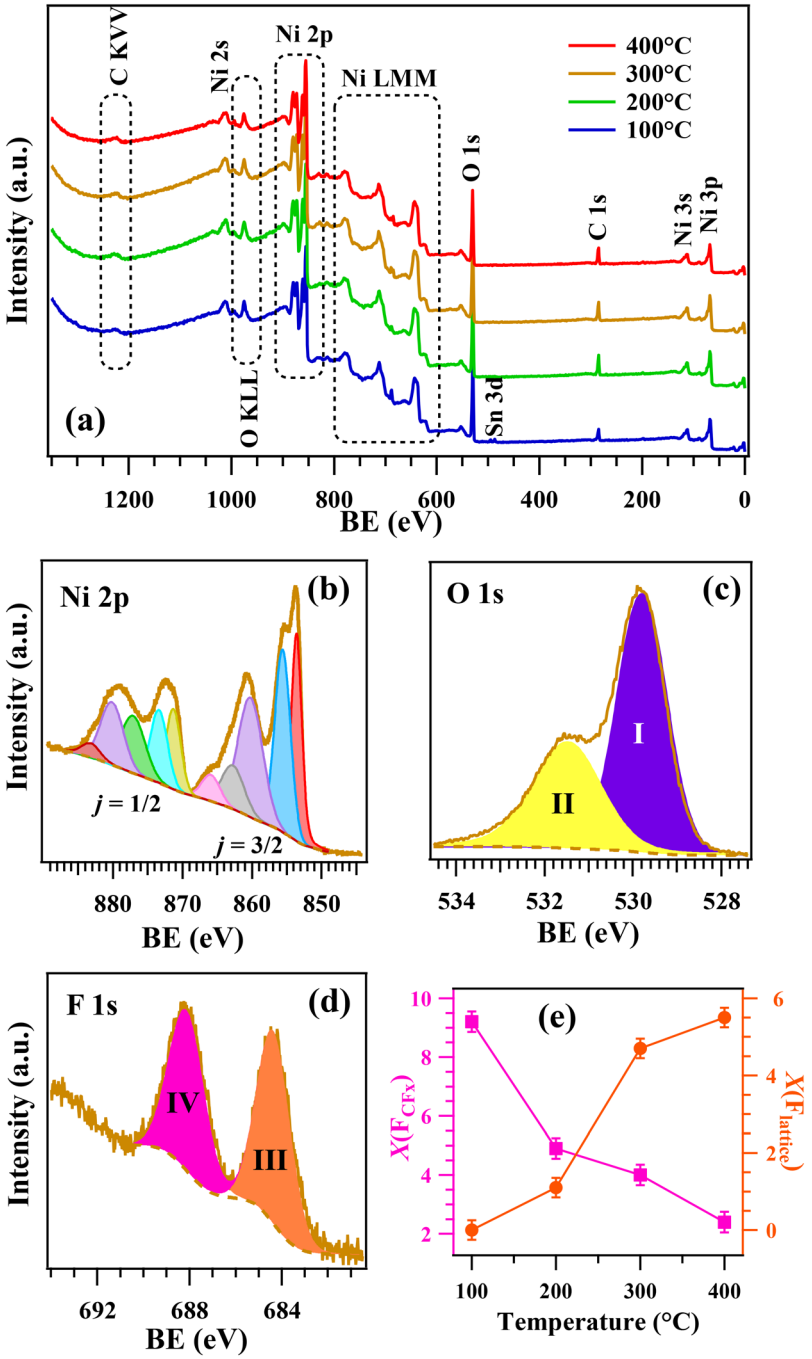

Fig. 3 (a) Surface wide-scan XPS surveys of NiO samples fabricated at different temperatures. Detailed Ni 2p (b), O 1s (c), and F 1s (d) regions for a specimen grown at 300 °C are also displayed. (e) Evolution of CF_x (pink points, left axis) and lattice F contributions (orange points, right axis) as a function of the growth temperature. $X(F_{CF_x})$ and $X(F_{lattice})$ were calculated as: $X(F_{CF_x})$ = [(at% F_{CF_x})/[(at% F_{CF_x}) + (at% Ni)]] × 100 and $X(F_{lattice})$ = [(at% $F_{lattice}$)/[(at% $F_{lattice}$) + (at% Ni)]] × 100.[36]

results confirmed the presence of fluorine in all specimens, with an overall average content estimated to be between 130 and 160 ppm, but its in-depth distribution was directly affected by the deposition temperature. Whereas at 100 °C an appreciable decrease of the corresponding signal took place throughout the outermost 400 nm, a more even F spatial distribution could be observed for the specimens grown at 300 °C and 400 °C. These results, in line with XPS (Fig. 3e and S6; Table S3, SI) and TEM outcomes (Fig. 7, 8, S11 and S12, SI), indicate that fluorine is mostly present in the near-surface regions in the form of CF_x groups at the lowest growth temperature. In a different way, the more even fluorine in-depth distribution upon increasing the thermal energy supply could be related to the higher lattice F content (see also above). Taken together, these outcomes indicate that, under suitable conditions, $Ni(tfa)_2TMEDA$ can be a

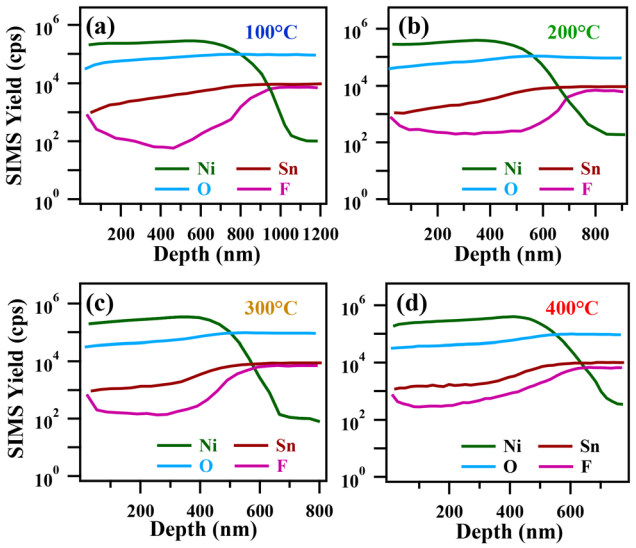

Fig. 4 SIMS depth profiles of specimens grown at 100 °C (a), 200 °C (b), 300 °C (c), and 400 °C (d).

single-source precursor for the PE-CVD of F-doped NiO, coherently with previous results for Mn_3O_4,[35] MnO_2,[34,37] Fe_2O_3,[38] Co_3O_4,[42] and NiO.[47]

The electronic properties of the fabricated systems were further investigated by reflection electron energy loss spectroscopy (REELS) and valence band analysis. The recorded REELS spectra (Fig. 5a) showed, beside the intense signal originating from elastic scattering of the incoming electrons centred at zero energy loss, a feature located between 1 and 2 eV, attributable to scattering collisions of the primary beam with hydrogen atoms in the material.[31,60] H content appeared to be qualitatively higher at the lowest deposition temperatures (100 °C and 200 °C). The onset of the anelastic background enabled to estimate the material band gap values, that turned out to be all very similar (Table S4, SI) and in line with literature values for NiO obtained by thermal CVD,[47] reactive sputtering[61] and solution routes.[62]

Fig. 5b reports the He(I) ultraviolet photoelectron spectroscopy (UPS) valence bands of NiO materials, whereas the corresponding XPS valence bands are displayed in Fig. S7, SI. Table S4, SI reports the extrapolated work function data, together with ionization potential and electron affinity values. The latter, affected in general by the adopted fabrication strategy and processing conditions,[47,63] were rather similar for the present materials. The calculated offset values of valence band edges from the Fermi level (E_F – VB) underscore, as expected, a p-type conductivity of the target specimens.[47] Based on these results, a tentative band scheme for the investigated nanomaterials is proposed in Fig. 5c. As can be observed, variations between the different specimens are quite modest, suggesting that their OER activities (see below, Fig. 9 and related comments) should be rather affected by other parameters and phenomena.

Preliminary morphological analyses were carried out by the combined use of field emission-scanning electron microscopy (FE-SEM) and atomic force microscopy (AFM; Fig. 6), that revealed a direct dependence of material features on the growth temperature. At 100 °C (Fig. 6a), the images were dominated by hierarchical quasi-one dimensional (1D) nanopillars [overall length = (800 ± 10) nm; lateral width = (40 ± 5) nm; aspect ratio = (800/40) = 20 ± 3]. The obtainment of this morphology can be traced back to the electrical field present at the plasma-sample interface, producing the observed anisotropic growth. Each pillar resulted by the aggregation of almost spherical nanoparticles (NPs) with a mean size of (25 ± 5) nm. These results, never reported, to the best of our knowledge, for nickel(II) oxide materials obtained by PE-CVD, underscore the plasma activation role in the formation of the target systems at low deposition temperatures. The assembly of such nanopillars resulted in the formation of an open area system, a favorable feature in view of the ultimate OER end-uses.[2,4–7,9] In fact, catalysts based on 1D nanomaterials can be deemed to be more efficient thanks to the large exposed surface and high density of active sites.[19]

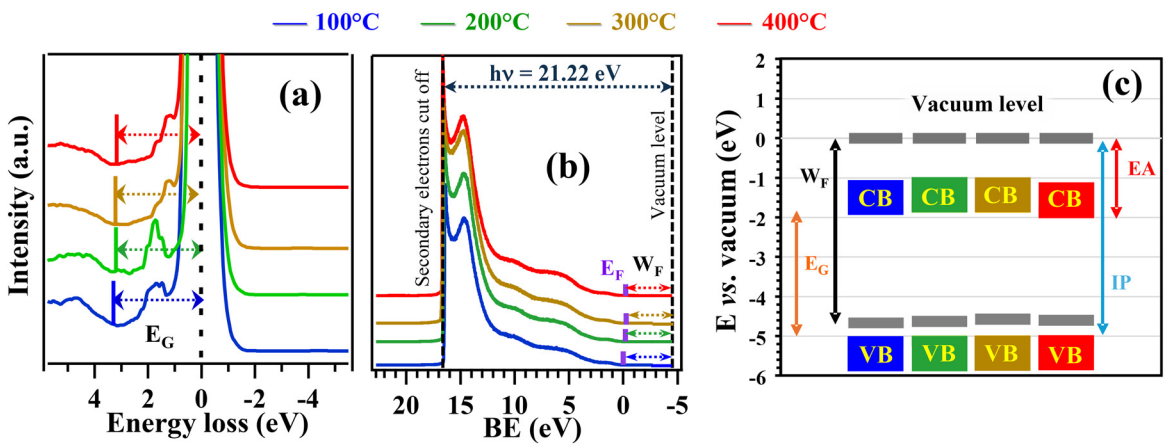

Fig. 5 (a) REELS spectra, (b) UPS valence bands and (c) energy level positions for the target systems with respect to the vacuum level (E_G = band gap; E_F = Fermi level energy; W_F = work function; CB = conduction band; VB = valence band; IP = ionization potential; EA = electron affinity).

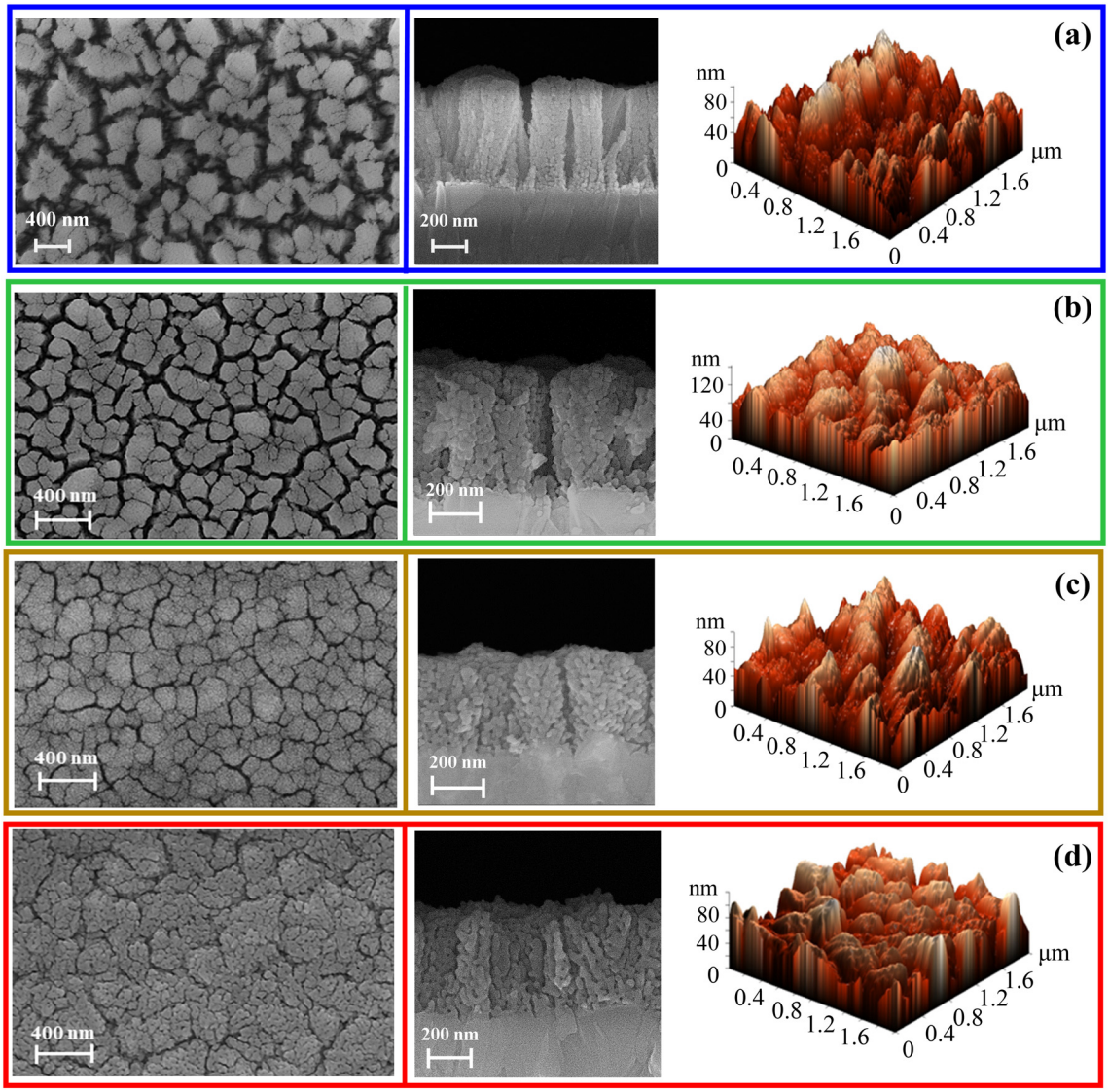

Fig. 6 Representative plane-view (left panel) and cross-sectional (central panel) FE-SEM images for NiO specimens deposited at 100 °C (a), 200 °C (b), 300 °C (c), and 400 °C (d). Right panel: 3D topographical AFM images for the same samples.

A relatively similar morphology could be observed even for the sample grown at 200 °C (Fig. 6b), although the formation of bigger and denser nanostructures yielded a less open cross-sectional arrangement. The overall deposit thickness underwent a reduction to (520 ± 10) nm, highlighting thus that an increase in the thermal energy supply renders lateral growth progressively competitive with the vertical one. This observation was corroborated by examining FE-SEM micrographs of specimens synthesized at 300 °C and 400 °C (Fig. 6c and d), which featured the interconnection of cauliflower-like structures and turned out to be more packed due to an enhanced lateral diffusion during material growth. For such systems, the deposit thickness was comprised between 470 nm and 500 nm. Cross-sectional line-scan energy dispersive X-ray spectroscopy (EDXS) profiles highlighted a very good compositional homogeneity, as demonstrated by the parallel trends of Ni Kα and O Kα signals throughout the deposit thickness (Fig. S8 and S9, SI). The specimen grown at 400 °C was characterized by F presence throughout the investigated depth, with a signal trend almost parallel to the Ni one (Fig. S9, SI), in line with SIMS results (see above and Fig. 4d). AFM images (Fig. 6, right panel and S10, SI) evidenced a granular surface topography for all systems, with a root-mean-square roughness of (17 ± 2) nm, regardless of the used growth temperature. This latter result could be attributed to the technique incapability of probing the whole material morphology throughout its profile, precluding thus the obtainment of significant differences for the target electrocatalysts.[31] In line with these observations, line scan profiles for the different specimens (Fig. S10, SI) were very similar.

In order to investigate in detail the system nanoscale structure, advanced TEM and related analyses were carried

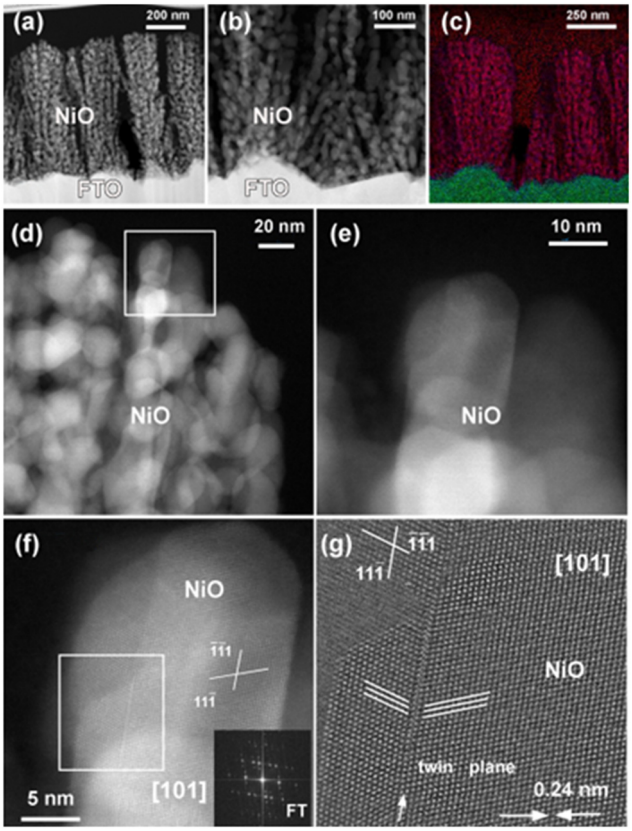

Fig. 7 (a) Low magnification HAADF-STEM cross-sectional image for a specimen grown at 100 °C. (b) Low magnification HAADF-STEM image of NiO/FTO interface. (c) EDXS-STEM elemental map showing Ni, O, and Sn distribution (color codes: Ni, red; O, blue; Sn, green). (d) Middle magnification micrograph of the outermost material region, and (e) high magnification HAADF-STEM micrograph of NiO grains framed by the white box in (d). (f) High resolution [101] HAADF-STEM image of NiO grain in (e) and corresponding Fourier transform (FT) pattern. (g) Magnified [101] HAADF-STEM image of the region selected by the white frame in (f). Twin ⟨111⟩ planes are evidenced by a white arrow, and the distance between ⟨111⟩ planes is marked.

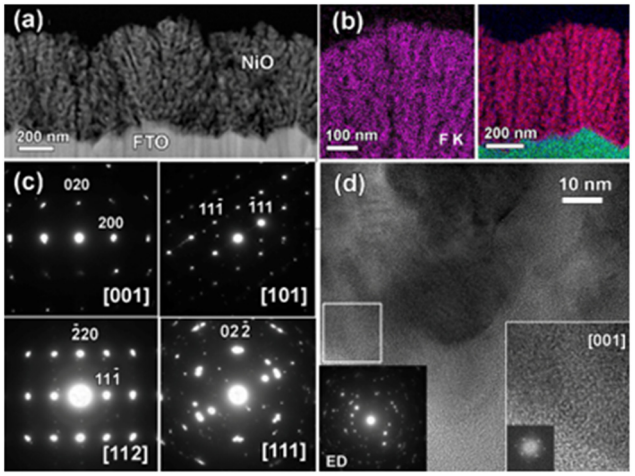

Fig. 8 (a) Low magnification HAADF-STEM cross-sectional image for a specimen deposited at 400 °C. (b) Corresponding EDXS-STEM elemental map of F K and overlaid color EDXS-STEM image showing Ni, O, and Sn distribution (color codes: Ni, red; O, blue; Sn, green). (c) ED patterns collected along the main crystallographic zone axes of NiO: [001], [101], [112], and [111]. (d) BF-HRTEM image of NiO grains and corresponding ED pattern. Inset: magnified [001] BF-HRTEM image of the region selected by the white frame, and corresponding Fourier transform (FT) pattern.

out on selected specimens fabricated at the lowest and highest deposition temperatures (Fig. 7 and 8). Low magnification high angle annular dark field-scanning TEM (HAADF-STEM) images and a simultaneously acquired EDXS-scanning TEM (EDXS-STEM) elemental map for the specimen fabricated at 100 °C are reported in Fig. 7a–c. As can be observed, the sample consists of NiO NPs (see also Fig. 7d), interconnected to form hierarchical quasi-1D pillars with an average length of (800 ± 10) nm, oriented almost perpendicularly to the underlying FTO substrate (Fig. 7b). The presence of these structures is consistent with FE-SEM results (Fig. 6). Nanoparticle bundles (200 ÷ 300 nm dimensional range, Fig. 7a), are separated by 50–100 nm voids, resulting thus in a high area nanoarchitecture, favorable for OER end-uses. NiO NPs have a typical average size of (30 ± 5) nm (Fig. 7d and e), and are ⟨111⟩– and ⟨100⟩-faceted (Fig. 7f and g).

According to the outcomes of EDXS-STEM analyses (see Fig. 7c and S11, SI), Ni and O are characterized by a homogeneous spatial distribution, and no segregation phenomena could be observed. Furthermore, high magnification and high resolution HAADF-STEM imaging enabled to rule out the occurrence of any secondary phase or amorphous layers at NPs surface and joint boundaries (Fig. 7e and f). These results confirmed the obtainment of cubic nickel(II) oxide (space group: $Fm\bar{3}m$[50]), in accordance with XRD results, with some NiO NPs exhibiting a twinned structure. As a representative case, Fig. 7f and g show an elongated twinned single NiO NP, with a width and length of (20 ± 2) and (40 ± 3) nm, respectively, and ⟨111⟩ twin planes, as typically observed for cubic structures. These twinnings were present in almost all NiO NPs for the target specimen, irrespective of the specific location.

At variance with the sample grown at 100 °C, presenting quasi-1D pillars, the one grown at 400 °C was characterized by interconnected, multi-granular cauliflower-like structures (Fig. 8a). As already mentioned, this difference was mainly ascribed to the enhanced thermal energy supply at higher substrate temperatures, resulting in the lateral growth being competitive with the vertical one, and leading to a more compact structure with a lower overall thickness [(520 ± 10) nm]. Even at 400 °C, no segregation phenomena or secondary phases could be evidenced, and EDXS-STEM mapping showed a homogeneous nickel and oxygen distribution. However, the 400 °C-grown sample presented an important difference with respect to the one obtained at 100 °C, related to the presence of evenly distributed fluorine (Fig. 8b and S12, SI), in accordance with the results of compositional analyses (see above). Electron diffraction (ED) analyses and bright field-high resolution TEM (BF-HRTEM)

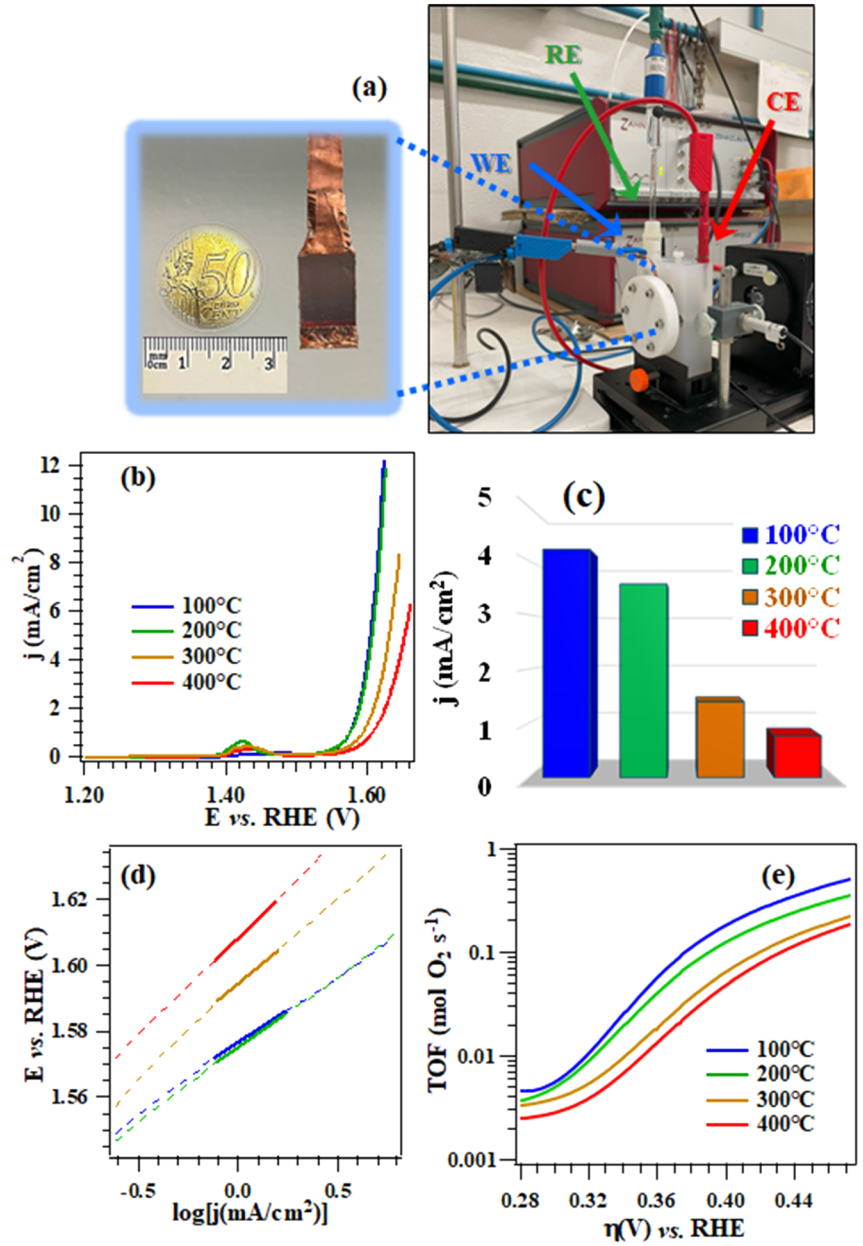

Fig. 9 (a) Photograph of the cell used for electrochemical tests (WE = working electrode; RE = reference electrode; CE = counter-electrode), with an enlargement of WE with the copper tape used for contacting. OER performances of NiO electrodes in alkaline water: (b) LSV curves for the target specimens. The peaks in the potential range 1.4–1.5 V correspond to the formation of NiO(OH),[16,17,20,27,28,32] whose occurrence is also supported by *ex situ* XPS analyses (see below). (c) Corresponding current density values at 1.6 V *vs.* RHE. (d) Tafel plots (dashed and continuous lines indicate experimental and fitting curves, respectively); (e) TOF *vs.* overpotential curves.

imaging (Fig. 8c and d) unambiguously confirmed the presence of cubic NiO as the sole crystalline phase and demonstrated ⟨111⟩/⟨100⟩ faceting, similar to the case of the 100 °C-grown specimen.

OER functional tests

The system OER electrocatalytic activity (Fig. 9a) was investigated in alkaline media. Fig. 9b displays the linear sweep voltammetry (LSV) curves for the NiO specimens fabricated at different temperatures, that evidenced a net current density increase at bias values >1.50 V *vs.* the reversible hydrogen electrode (RHE). The data clearly indicate that the best performing sample is the one grown at 100 °C, and that material OER activities varied according to the following trend: 100 °C > 200 °C > 300 °C > 400 °C (Fig. 9b and c). This trend finds its counterpart in the measured Tafel slopes (Fig. 9d and Table S5, SI), that underwent a progressive decrease upon going from the 400 °C to the 100 °C-grown sample. Since lower Tafel slopes correspond to an enhanced OER kinetics,[2,7] these results underscore the improved performances of electrocatalysts fabricated at the lowest temperatures, in particular of the 100

°C one. Remarkably, the actual Tafel slope values and the performances of the target systems compared favourably with various Ni-based electrocatalysts reported so far (see Table S5, SI, and related references). The above indicated reactivity trend was consistent with the information provided by the turnover frequency (TOF), that was considered for a better investigation of the intrinsic electrocatalyst OER activity.[8] The relationship between TOF and overpotential (η) (Fig. 9e) confirmed the superior performance of the 100 °C-grown specimen during the entire OER regime. The calculated TOF value for an overpotential of 400 mV *vs.* RHE increased from (0.050 ± 0.005) s^{-1} to (0.18 ± 0.05) s^{-1} upon going from the 400 °C sample to the 100 °C one. For the latter, the TOF value was appreciably higher than those reported for NiO nanofibers,[19] NiO nanowall electrocatalysts,[8] and Ni/NiO nanocomposites,[13] highlighting thus the validity and applicative potential of the present results.

The best performances of the 100 °C-grown sample in the target electrocatalyst family can be attributed to the synergy of different phenomena. The main one is linked to morphology-related transport properties. Specifically, despite the higher thickness in comparison to the 400 °C-grown electrocatalyst, the 100 °C-grown specimen features a more open structure. Thus, the higher active area favours the access of reactant molecules to Ni active sites and the subsequent product outdiffusion.[19,25,58] Accordingly, travel distances of charge carriers are reduced, minimizing thus detrimental electron–hole recombination and yielding an improved OER activity.[7] An additional contributing effect relates to the higher microstrain and dislocation density obtained for this specimen. In fact, by disrupting the equilibrium of interatomic bonds at metal sites, a faster adsorption/dissociation kinetics of the incoming oxygen molecules occurs, resulting thus in an improved electrocatalytic activity.[49]

Another important difference between the target electrocatalysts is related to the different types and relative contents of F-containing moieties. Indeed, as highlighted by compositional data (see above and Fig. 3e), fluorine was present both in Ni-F bonds and in precursor-derived CF_x groups, corresponding respectively to components (III) and (IV) in Fig. 3d and S6 in the SI, with (IV) being the only contribution for the sample grown at 100 °C. These CF_x groups have a direct influence on electrocatalytic activity, as explained below. Any significant influence of oxygen vacancy content on the different activities of the investigated materials could be unambiguously ruled out, since, as observed above, O/Ni at% ratios were very close for all the target systems.

Results on the catalyst stability, a critical factor in view of eventual real-world applications,[11,14,29] are reported in the SI (see Fig. S13 and S14). As can be observed in Fig. S13, SI, after an initial induction period in which the slight current density decrease might be related to the generated O_2 bubbles, which did not leave the surface immediately during gas generation,[28] both the specimens grown at 100 °C and 400 °C present rather constant performances upon prolonged utilization. On this basis, the occurrence of relevant degradation/poisoning phenomena was ruled out, as also supported by the negligible variations featured by LSV curves (Fig. S14a, SI) and the calculated Tafel slopes after long-term stability tests (Fig. S14b, SI; compare with the values of the pristine electrocatalysts reported in Table S5, SI).

Coherently with the above results, *post-operando* XRD and FE-SEM investigation after prolonged electrochemical tests evidenced that the system structure and morphology did not undergo appreciable alterations (compare Fig. S16, SI with Fig. 2a and S17, SI with Fig. 6). It is worthwhile noticing that interaction with the KOH electrolyte leads to the surface formation of $Ni(OH)_2$ and NiO(OH),[27,32] as indicated by the XPS signals of Ni 2p and O 1s acquired after functional tests. In fact, for both the specimens grown at 100 °C and 400 °C, this conclusion is supported by the Ni 2p lineshape variation and by the intensity increase of component (II) in the O 1s peak (see Fig. S18 and S19, SI).[8,16,54] This phenomenon was accompanied by the appearance of band (III) in the O 1s photopeak (see Table S6, SI), related to adsorbed water,[8,16,55] as well as by an increase of the CF_x contribution to the overall F 1s signal for the 400 °C-grown sample (compare Tables S3 and S7, SI). Nevertheless, the overall fluorine content (≈4 at%) does not show any appreciable decrease after prolonged testing (Fig. S20, SI), enabling thus to rule out any substantial fluorine dissolution during OER. These results are in tune with the above indications and enable to discard any significant long-term performance decay.

To rationalize the obtained results, hydroxylated NiO surfaces exhibiting CF_x groups and both reticular F (F_r) and adsorbed CF_x groups – mimicking samples grown at $T = 100$ °C and $T > 100$ °C, respectively – were modelled (S2 and S6, SI). For sake of completeness, models characterized by different compositions of precursor-derived CF_x moieties (namely CF_3, CF_2, and CF) were initially investigated (Fig. S1, SI). Only the CF-containing models featured properties compatible with the p-type nature of the deposited materials (Table S9 and Fig. S22, SI), suggesting therefore that the most likely composition of CF_x moieties should be CF. These CF groups are more favorably adsorbed on top-layer Ni sites (Ni*) directly bonded to –OH groups, as indicated by the minimum energy structures calculated for the NiO(CF) and $NiOF_r$(CF) models (Fig. 10a and b, respectively). As can be observed, in both cases CF binding on Ni* cations results in significant structural changes on NiO surface, in particular regarding the local environment of Ni* sites (see also S7 and Fig. S23a, SI). In particular, Ni* cations are up-shifted by ≈1 Å with respect to the other top-layer Ni atoms. As a result, Ni* are bonded to two nearest-neighbour O atoms, an effect slightly more pronounced in the NiO(CF) model, *i.e.* in the absence of F_r (Fig. 10a, S1c, and S21, SI). Hence, Ni* sites exhibit a nearly planar three-coordinated environment, suggesting that Ni*-CF moieties could be characterized by a high reactivity in the OER process. In addition, even top-layer reticular F_r – which replace surface O atoms – are up-shifted by 1.2 Å with respect to top-layer oxygen (Fig. 10b), indicating that they could be prone to contact with incoming reactants.

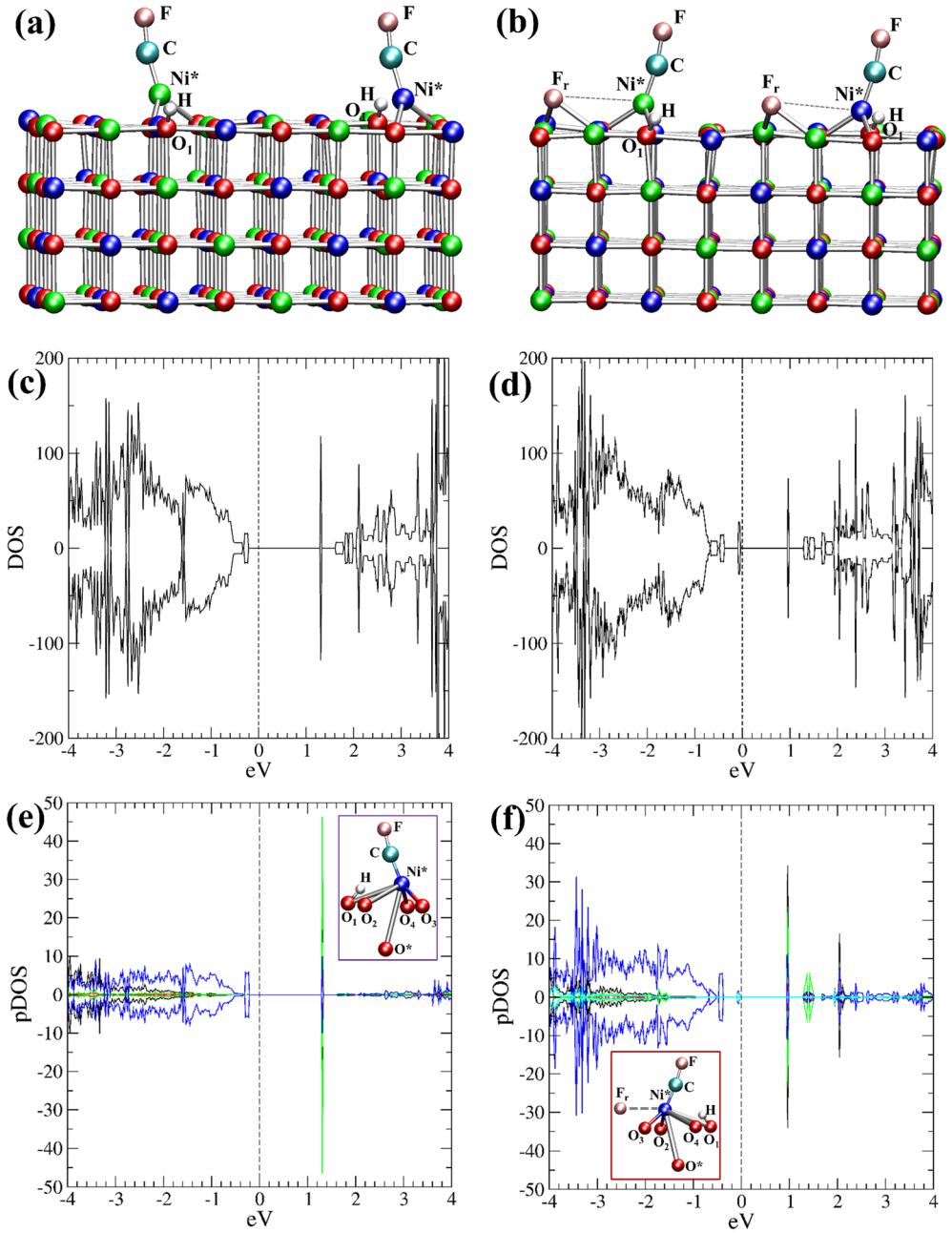

Fig. 10 Minimum energy structures calculated for: (a) NiO(CF); (b) $NiOF_r(CF)$. Atom color codes: blue = Ni (spin up); green = Ni (spin down); red = O; pink = F; cyan = C; white = H. Ni*: Ni atoms bearing the –CF group; O_1: hydroxyl oxygens; F_r: reticular F atoms. c and d) DOS for: (c) NiO(CF); (d) $NiOF_r(CF)$. Vertical dashed line: Fermi level position. Positive curves: spin-up components; negative curves: spin-down components. e and f) pDOS for: (e) NiO(CF); (f) $NiOF_r(CF)$. Black: Ni* d-states; red: $F_{(CF)}$ 2p states; green: C 2p states; blue: nearest-neighbour O atoms 2p states; cyan: F_r 2p states. Insets: representation of the Ni* environment.

To elucidate the role of Ni*CF and F_r defects in electrocatalysis, the electronic structures of NiO(CF) and $NiOF_r(CF)$ models were analyzed by calculating the corresponding density of states (DOS, Fig. 10c and d), and the projected DOS (pDOS, Fig. 10e and f). Remarkably, CF presence yields the appearance of a high density of empty states above the Fermi level at 1.32 eV and 0.98 eV for NiO(CF) and $NiOF_r(CF)$, respectively (Fig. 10c and d). Indeed, the formation of these new, easily accessible empty electronic states – absent for the pristine NiO surface (Fig. S23b, SI) - might be the atomistic origin of OER activity for the present electrocatalysts, since they could accept electron density from incoming OH^- anions. A careful pDOS inspection reveals that these states are mainly localized not only on the Ni*-CF moiety, but also on the nearest-neighbour O atoms – *i.e.*, on the local environment of the Ni* site (Fig. 10e and f). Notably, the density of such empty states is significantly higher for NiO(CF) than for $NiOF_r(CF)$, indicating that NiO surfaces with

adsorbed CF moieties might be more efficient OER catalysts in comparison to the ones featuring both surface-adsorbed CF and F incorporation into NiO lattice. Conversely, the presence of reticular F is associated to the formation of new occupied states immediately below the Fermi level, essentially localized on F_r 2p-states (Fig. 10d and f), and does not generate new low-energy empty states, which would favourably boost the OER process.

Conclusions

In this work, we have reported on the PE-CVD of NiO nanoarchitectures from a fluorinated Ni(II) diketonate-diamine molecular source in Ar–O_2 plasmas on FTO substrates. The outcomes of a comprehensive experimental and theoretical characterization evidenced the successful formation of NiO nanosystems with tailored features, showing a morphology tuneable from hierarchical quasi-1D pillars to cauliflower-like structures as a function of the growth temperature. Variation of the latter in the 100–400 °C interval enabled also to modulate the nature of the incorporated fluorine from surface CF_x groups to homogeneously distributed F in NiO lattice. These variations were directly reflected from the resulting OER electrocatalytic performances, that turned out to be the best for the 100 °C system (Tafel slope value as low as 39 mV × dec^{-1}; overpotential of 390 mV to achieve a current density of 10 mA × cm^{-2}). The actual performances are well positioned in the current panorama of Ni(II) oxide OER electrocatalysts. An experimental and theoretical investigation enabled us to account for this achievement in terms of material morphology, enabling an easier transport of charge carriers and favoring reactant and products diffusion for high area quasi-1D structures. Additional concurring contributions were related to the higher content of structural defects and to the type of incorporated fluorine in the fabricated materials. In this context, the present outcomes suggest that surface CF moieties, significantly modifying NiO electronic structure through the creation of new intra-gap empty states, could represent the atomistic origin of an enhanced OER activity. Altogether, our results disclose challenging perspectives towards the engineering of electrocatalysts based on non-precious materials for sustainable energy conversion. Additional research developments will concern evaluation of the Faradaic efficiency for oxygen evolution from the target systems, as well as the fabrication of heterostructured architectures even on different substrates for wastewater treatment and electrochemical valorization of various oxygenates, for instance in urea electrosynthesis.[64,65]

Experimental

Material synthesis

PE-CVD growth processes were carried out from Ar–O_2 plasmas using a custom-built capacitively-coupled two-electrode instrumentation equipped with a radio frequency (RF) generator (nominal frequency ν = 13.56 MHz; maximum power input = 300 W). Ni(tfa)$_2$TMEDA, a monomeric complex with a pseudo-octahedral coordination of Ni(II) centers, endowed with favorable properties for CVD applications, was used as molecular precursor.[66,67] FTO-coated glass substrates (Aldrich®; ≈7 Ω × sq^{-1}; FTO thickness ≈600 nm), subjected to an established pre-cleaning procedure,[56] were mounted on the ground electrode, whereas RF-power was delivered to the second electrode. A matching unit, equipped with a load (C_L) and a tune (C_T) variable capacitors, interposed between the generator and the RF-electrode, was used to automatically tune reflected power to zero. In each experiment, the precursor powders [mass = (0.15 ± 0.05) g] were placed in an external glass vessel heated at (75 ± 1) °C by means of an external oil bath, and its vapors were transported into the reaction chamber by an Ar flow [rate = (60 ± 1) standard cubic centimeters per minute (sccm)] through heated gas lines maintained at (150 ± 2) °C to avoid detrimental condensation losses. Two independent gas lines were used to introduce Ar [rate = (15 ± 1) sccm] and O_2 [rate = (5 ± 1) sccm] directly into the reaction chamber. For all depositions, the interelectrode distance, RF-power, process duration, and total pressure were set at (6.0 ± 0.5) cm, (20 ± 2) W, (90 ± 1) min, and (1.0 ± 0.3) mbar, respectively. Under these conditions, a self-bias potential ($|V_{bias}|$) of (170 ± 10) V developed at the RF-electrode, with typical C_T and C_L values of (335 ± 5) and (625 ± 5) pF, respectively. The growth temperature varied between (100 ± 2) °C and (400 ± 2) °C in different experiments. Before characterization, all the obtained samples were subjected to *ex situ* annealing in air at (550 ± 2) °C for (60 ± 1) min.

Material characterization

XRD measurements were carried out by using a Panalytical Empyrean diffractometer, operating in Bragg–Brentano (BB) mode, using a Cu Kα X-ray source (λ = 1.54056 Å) powered at 40 kV and 40 mA. The instrument is equipped with a Pix-Cel two-dimensional detector for BB acquisitions with a 255 × 255 array sensor, covering a 3° × 3° solid angle. The uncertainty on the actual angular positions was ±0.1°. XPS, UPS, and REELS analyses were performed using a Thermo Fisher ESCALAB QXi apparatus equipped with a monochromatic Al Kα X-ray source ($h\nu$ = 1486.6 eV). The reported BEs (standard deviation = ± 0.2 eV) were corrected for charging by assigning a value of 284.8 eV to the adventitious C 1s signal[23,54] (C_0 in Fig. S3, SI). Atomic percentages (at%; uncertainties: ±0.5%) were calculated by signal integration using ThermoFisher sensitivity factors. REELS and UPS analyses were carried out using a primary electron beam energy of 1.0 keV and a UV He(I) ($h\nu$ = 21.22 eV) photon source, respectively. The estimation of material band gap was performed from REELS spectra, using the package provided by ThermoScientific Avantage software (version 6.9.1, Build 00004), after subtraction of the elastic peak. SIMS measurements were run on an IMS 4f instrument (Cameca), using a Cs^+ primary ion beam (14.5 keV, 35 nA;

stability < 0.3%) and by negative secondary ion detection, performing charge compensation by an electron gun. Analyses were conducted in beam blanking mode rastering over a 175 × 175 μm^2 area and collecting secondary ions from a 7 × 7 μm^2 sub-region to avoid crater effects. The erosion time was converted into depth using thickness values evaluated from cross-sectional FE-SEM analyses. FE-SEM and EDXS characterization was performed using a Zeiss SUPRA 40 VP instrument equipped with an INCA x-act pentaFET Precision spectrometer, operating at primary beam voltages of 10–20 kV. The average nanoparticle sizes were evaluated by a statistical image analysis. An NT-MDT SPM Solver P47H-PRO apparatus, operated in tapping mode and in air, was employed for AFM characterization. TEM, ED, and EDXS elemental mapping experiments were carried out using an aberration double-corrected cold FEG JEM ARM200F microscope operated at 200 kV, equipped with a CENTURIO EDXS detector, an ORIUS Gatan camera and a Quantum GIF.

Functional tests

Electrocatalytic activity tests were performed at room temperature in 1.0 M KOH solutions (pH ≈ 14.0) using an integrated potentiostatic instrumentation consisting of a Zennium-PRO and a PP212 unit from Zahner GmbH, coupled with an optical bench containing a Zahner electrochemical cell. FTO-supported NiO systems were employed as working electrodes, whereas a MMO (Hg/HgO) electrode and a Pt coil were used as reference and counterelectrode, respectively. LSV traces were recorded at a constant scan rate of 1 mV × s^{-1}. Tafel slopes were calculated by plotting the overpotential *vs.* RHE against log(current density).[68,69] Chronoamperometry (CA) analyses were carried out at 1.60 V *vs.* RHE.

Theoretical calculations

Structural and electronic properties of F-doped NiO(100) slab models were investigated with a computational strategy based on Density Functional Theory (DFT) and complemented by a Hubbard Hamiltonian[70] approach. The slab systems used in the present work were built starting from hydroxylated NiO(100) models (simulation cell stoichiometry: $Ni_{64}O_{64}H_2$) constituted by four NiO layers and a 14 Å vacuum space.[71] F-doping was simulated by adding to these models CF_x-defects on top-layer Ni atoms (x = 3, 2, 1), and by replacing top-layer O atoms with F atoms (see S2 and Fig. S1 in the SI). To treat the ion-core electron interactions, ultra-soft pseudopotentials[72,73] were used for all atoms. Geometry optimizations were performed using the unrestricted PBE functional,[74] yielding a good structural description of metal-oxide material surfaces.[75] An empirical treatment of dispersion interactions (D3-bj)[76] was adopted. The valence electrons considered in this work were: Ni $3s^2 3p^6 3d^8 4s^2$; F $2s^2 2p^5$; O $2s^2 2p^4$; C $2s^2 2p^2$; H $1s^1$. All calculations were characterized by a plane-wave basis set with a 40 Ry cutoff for the wavefunction (320 Ry for the electron density), along with a 1 × 2 × 1 mesh for the Brillouin Zone sampling. Electronic structure and magnetization calculations were performed on minimum energy structures with DFT+U,[77] introducing a Hubbard U term of 6.4 eV,[71] and giving opposite signs to the initial spin polarizations of spin-up and spin-down Ni atoms. A self-consistent protocol for magnetization calculation was adopted, as pertinent to the treatment of magnetic oxide-based materials.[78,79] The electronic structure character of each slab model (*e.g.*, n-type, p-type, metallic,…) was established by comparing VB and CB band edges with the Fermi energy.[80,81] Convergence control of the basis set for the electronic structure was performed by adopting a plane-wave cutoff of 60 Ry (see Fig. S22a, SI).

Additional details on material preparation, characterization, and modeling are reported in the SI.

Author contributions

C. M.: conceptualization, writing – original draft preparation, supervision and resources. D. B.: methodology, investigation, supervision and resources, writing – reviewing and editing. L. S.: investigation, writing – reviewing and editing. E. S.: methodology, investigation, data curation. G. T. and E. F.: conceptualization, investigation, methodology, writing – original draft. C. S.: methodology, data curation, writing – reviewing and editing. O. I. L. and E. M.: investigation and data curation. A. G.: methodology, investigation, data curation, writing – reviewing and editing. E. P.: investigation, data curation. N. E. H.: investigation, data curation, writing – original draft. G. A. R.: methodology, conceptualization and investigation.

Conflicts of interest

All the authors declare they have no competing interest.

Data availability

Supplementary information is available. See DOI: **https://doi.org/10.1039/D5CY00833F**.

The data supporting this article are included as part of the SI.

Acknowledgements

The authors gratefully acknowledge financial support from the National Research Council (Progetti di Ricerca @CNR-avviso 2020-ASSIST), Padova University (PDiSC#02BIRD2023-UNIPD RIGENERA, DOR 2023–2025), INSTM Consortium (INSTM Consortium (TRI.25/013-CIMENTO)), PRIN 2022474YE8 (SCI-TROPHY project; Next Generation EU - Bando PRIN 2022 – M4.C2.1.1), and Insubria University (FAR2024).

Notes and references

1 **https://www.mckinsey.com/industries/energy-and-materials/our-insights/global-energy-perspective**.

2 P. T. Babar, A. C. Lokhande, M. G. Gang, B. S. Pawar, S. M. Pawar and J. H. Kim, *J. Ind. Eng. Chem.*, 2018, **60**, 493–497.
3 Z. Guo, X. Wang, Y. Gao and Z. Liu, *Dalton Trans.*, 2020, **49**, 1776–1784.
4 K. Hemmati, A. Kumar, A. R. Jadhav, O. Moradlou, A. Z. Moshfegh and H. Lee, *ACS Catal.*, 2023, **13**, 5516–5528.
5 C. Qin, S. Tian, Z.-J. Jiang, M. Thandavarayan and Z. Jiang, *Electrochim. Acta*, 2023, **449**, 142179.
6 T. Zahra, K. S. Ahmad, C. Zequine, R. K. Gupta, A. Guy Thomas and M. Azad Malik, *Sustain. Energy Technol. Assess.*, 2020, **40**, 100753.
7 L. Bigiani, C. Maccato, T. Andreu, A. Gasparotto, C. Sada, E. Modin, O. I. Lebedev, J. R. Morante and D. Barreca, *ACS Appl. Nano Mater.*, 2020, **3**, 9889–9898.
8 S. Cosentino, M. Urso, G. Torrisi, S. Battiato, F. Priolo, A. Terrasi and S. Mirabella, *Mater. Adv.*, 2020, **1**, 1971–1979.
9 Q. Dong, C. Sun, Z. Dai, X. Zang and X. Dong, *ChemCatChem*, 2016, **8**, 3484–3489.
10 S. G. Jo, C.-S. Kim, S. J. Kim and J. W. Lee, *Nanomaterials*, 2021, **11**, 3379.
11 J. P. Kumar, S. D. Giri and A. Sarkar, *Int. J. Hydrogen Energy*, 2018, **43**, 15639–15649.
12 R. K. Mishra, V. Kumar, G. J. Choi, J. W. Ryu, S. M. Mane, J. C. Shin and J. S. Gwag, *Mater. Lett.*, 2022, **324**, 132740.
13 N. Srinivasa, J. P. Hughes, P. S. Adarakatti, C. Manjunatha, S. J. Rowley-Neale, S. Ashoka and C. E. Banks, *RSC Adv.*, 2021, **11**, 14654–14664.
14 Z. Wu, Z. Zou, J. Huang and F. Gao, *J. Catal.*, 2018, **358**, 243–252.
15 L. Hou, X. Gu, X. Cui, J. Tang, Z. Li, X. Liu and J. Cho, *EES Catal.*, 2023, **1**, 619–644.
16 A. R. Blume, W. Calvet, A. Ghafari, T. Mayer, A. Knop-Gericke and R. Schlögl, *Phys. Chem. Chem. Phys.*, 2023, **25**, 25552–25565.
17 E. Arciga-Duran, Y. Meas, J. J. Pérez-Bueno, J. C. Ballesteros and G. Trejo, *Electrochim. Acta*, 2018, **268**, 49–58.
18 C. Maccato, L. Bigiani, L. Girardi, A. Gasparotto, O. I. Lebedev, E. Modin, D. Barreca and G. A. Rizzi, *Adv. Mater. Interfaces*, 2021, **8**, 21700763.
19 V. D. Silva, T. A. Simões, J. P. F. Grilo, E. S. Medeiros and D. A. Macedo, *J. Mater. Sci.*, 2020, **55**, 6648–6659.
20 L.-A. Stern and X. Hu, *Faraday Discuss.*, 2014, **176**, 363–379.
21 M. Yang, H. Zhu, Y. Zheng, C. Zhang, G. Luo, Q. Xu, Q. Li, S. Zhang, T. Goto and R. Tu, *RSC Adv.*, 2022, **12**, 10496–10503.
22 A. Kundu, B. Kumar, A. Rajput and B. Chakraborty, *ACS Appl. Mater. Interfaces*, 2023, **15**, 8010–8021.
23 Z. Qiu, Y. Ma and T. Edvinsson, *Nano Energy*, 2019, **66**, 104118.
24 Z. Li, W. Niu, L. Zhou and Y. Yang, *ACS Energy Lett.*, 2018, **3**, 892–898.
25 K. Fominykh, J. M. Feckl, J. Sicklinger, M. Döblinger, S. Böcklein, J. Ziegler, L. Peter, J. Rathousky, E.-W. Scheidt, T. Bein and D. Fattakhova-Rohlfing, *Adv. Funct. Mater.*, 2014, **24**, 3123–3129.
26 S. Haghverdi Khamene, C. van Helvoirt, M. N. Tsampas and M. Creatore, *J. Phys. Chem. C*, 2023, **127**, 22570–22582.
27 C. Hu, K. Chu, Y. Zhao and W. Y. Teoh, *ACS Appl. Mater. Interfaces*, 2014, **6**, 18558–18568.
28 H. Sun, Z. Ma, Y. Qiu, H. Liu and G.-g. Gao, *Small*, 2018, **14**, 1800294.
29 T. Yu, Q. Xu, L. Luo, C. Liu and S. Yin, *Chem. Eng. J.*, 2022, **430**, 133117.
30 M. Bonomo, *J. Nanopart. Res.*, 2018, **20**, 222.
31 D. Barreca, E. Scattolin, C. Maccato, A. Gasparotto, L. Signorin, N. El Habra, A. Šuligoj, U. L. Štangar and G. A. Rizzi, *Chem. Commun.*, 2025, **61**, 2945–2948.
32 C. Lin, Y. Zhao, H. Zhang, S. Xie, Y.-F. Li, X. Li, Z. Jiang and Z.-P. Liu, *Chem. Sci.*, 2018, **9**, 6803–6812.
33 C. Maccato, L. Bigiani, G. Carraro, A. Gasparotto, R. Seraglia, J. Kim, A. Devi, G. Tabacchi, E. Fois, G. Pace, V. Di Noto and D. Barreca, *Chem. – Eur. J.*, 2017, **23**, 17954–17963.
34 D. Barreca, G. Carraro, E. Fois, A. Gasparotto, F. Gri, R. Seraglia, M. Wilken, A. Venzo, A. Devi, G. Tabacchi and C. Maccato, *J. Phys. Chem. C*, 2018, **122**, 1367–1375.
35 L. Bigiani, D. Barreca, A. Gasparotto, C. Sada, S. Martí-Sanchez, J. Arbiol and C. Maccato, *CrystEngComm*, 2018, **20**, 3016–3024.
36 D. Barreca, F. Gri, A. Gasparotto, G. Carraro, L. Bigiani, T. Altantzis, B. Žener, U. Lavrenčič Štangar, B. Alessi, D. B. Padmanaban, D. Mariotti and C. Maccato, *Nanoscale*, 2019, **11**, 98–108.
37 D. Barreca, F. Gri, A. Gasparotto, T. Altantzis, V. Gombac, P. Fornasiero and C. Maccato, *Inorg. Chem.*, 2018, **57**, 14564–14573.
38 G. Carraro, A. Gasparotto, C. Maccato, E. Bontempi, O. Lebedev, S. Turner, C. Sada, L. E. Depero, G. Van Tendeloo and D. Barreca, *RSC Adv.*, 2013, **3**, 23762–23768.
39 D. Barreca, G. Carraro, A. Devi, E. Fois, A. Gasparotto, R. Seraglia, C. Maccato, C. Sada, G. Tabacchi, E. Tondello, A. Venzo and M. Winter, *Dalton Trans.*, 2012, **41**, 149–155.
40 D. Barreca, L. Bigiani, M. Klotzsche, A. Gasparotto, R. Seraglia, C. Jandl, A. Pöthig, E. Fois, L. Vanin, G. Tabacchi, M. Roverso, S. Bogialli, E. Callone, S. Dirè and C. Maccato, *Mater. Chem. Phys.*, 2022, **277**, 125534.
41 M. Klotzsche, D. Barreca, L. Bigiani, R. Seraglia, A. Gasparotto, L. Vanin, C. Jandl, A. Pöthig, M. Roverso, S. Bogialli, G. Tabacchi, E. Fois, E. Callone, S. Dirè and C. Maccato, *Dalton Trans.*, 2021, **50**, 10374–10385.
42 A. Gasparotto, D. Barreca, D. Bekermann, A. Devi, R. A. Fischer, P. Fornasiero, V. Gombac, O. I. Lebedev, C. Maccato, T. Montini, G. Van Tendeloo and E. Tondello, *J. Am. Chem. Soc.*, 2011, **133**, 19362–19365.
43 A. Gasparotto, D. Barreca, D. Bekermann, A. Devi, R. A. Fischer, C. Maccato and E. Tondello, *J. Nanosci. Nanotechnol.*, 2011, **11**, 8206–8213.
44 M. Chandrakala, S. Raj Bharath, T. Maiyalagan and S. Arockiasamy, *Mater. Chem. Phys.*, 2017, **201**, 344–353.
45 N. Weidler, J. Schuch, F. Knaus, P. Stenner, S. Hoch, A. Maljusch, R. Schäfer, B. Kaiser and W. Jaegermann, *J. Phys. Chem. C*, 2017, **121**, 6455–6463.
46 E. Fujii, A. Tomozawa, H. Torii and R. Takayama, *Jpn. J. Appl. Phys.*, 1996, **35**, L328–L330.

47 M. Benedet, C. Maccato, G. Pagot, C. Invernizzi, C. Sada, V. Di Noto, G. A. Rizzi, E. Fois, G. Tabacchi and D. Barreca, *J. Phys. Chem. C*, 2023, **127**, 22304–22314.
48 J. Zhai, T. Dong, Y. Zhou, J. Min, Y. Yan, C. S. Garoufalis, S. Baskoutas, D. Xu and Z. Zeng, *Nano Lett.*, 2023, **23**, 3239–3244.
49 Z. Hou, C. Cui, Y. Li, Y. Gao, D. Zhu, Y. Gu, G. Pan, Y. Zhu and T. Zhang, *Adv. Mater.*, 2023, **35**, 2209876.
50 Pattern No. 00-0047-1049, JCPDS, 2000.
51 F. Hajakbari, *J. Nanostruct. Chem.*, 2020, **10**, 97–103.
52 A. H. Hammad, M. S. Abdel-wahab, S. Vattamkandathil and A. R. Ansari, *Phys. B*, 2019, **568**, 6–12.
53 A. A. Ahmed, M. Devarajan and N. Afzal, *Mater. Sci. Semicond. Process.*, 2017, **63**, 137–141.
54 B. P. Payne, M. C. Biesinger and N. S. McIntyre, *J. Electron Spectrosc. Relat. Phenom.*, 2009, **175**, 55–65.
55 G. Pagot, M. Benedet, C. Maccato, D. Barreca and V. Di Noto, *Surf. Sci. Spectra*, 2023, **30**, 024028.
56 D. Barreca, G. Carraro, A. Gasparotto, C. Maccato, C. Sada, A. P. Singh, S. Mathur, A. Mettenbörger, E. Bontempi and L. E. Depero, *Int. J. Hydrogen Energy*, 2013, **38**, 14189–14199.
57 K. Zhu, F. Shi, X. Zhu and W. Yang, *Nano Energy*, 2020, **73**, 104761.
58 N. Hussain, W. Yang, J. Dou, Y. Chen, Y. Qian and L. Xu, *J. Mater. Chem. A*, 2019, **7**, 9656–9664.
59 F. Zhang, R. Ji, Y. Liu, Z. Li, Z. Liu, S. Lu, Y. Wang, X. Wu, H. Jin and B. Cai, *Chem. Eng. J.*, 2020, **401**, 126037.
60 S. D. Nehate, A. K. Saikumar and K. B. Sundaram, *Coatings*, 2021, **11**, 196.
61 M. I. Pintor-Monroy, B. L. Murillo-Borjas, M. Catalano and M. A. Quevedo-Lopez, *ACS Appl. Mater. Interfaces*, 2019, **11**, 27048–27056.
62 E. L. Ratcliff, J. Meyer, K. X. Steirer, A. Garcia, J. J. Berry, D. S. Ginley, D. C. Olson, A. Kahn and N. R. Armstrong, *Chem. Mater.*, 2011, **23**, 4988–5000.
63 M. A. Hidrogo-Rico, N. Nedev, P. Horley, M. I. Mendívil, J. Castillo-Saenz, E. Martínez-Guerra, E. J. Juarez-Perez, F. S. Aguirre-Tostado, A. Susarrey-Arce and E. Martínez-Guerra, *ACS Omega*, 2025, **10**, 422–438.
64 W. Du, Z. Sun, K. Chen, Y. Wei, R. Bao and K. Chu, *Adv. Energy Mater.*, 2024, **14**, 2401765.
65 K. Chen, D. Ma, Y. Zhang, F. Wang, X. Yang, X. Wang, H. Zhang, X. Liu, R. Bao and K. Chu, *Adv. Mater.*, 2024, **36**, 2402160.
66 M. Benedet, D. Barreca, E. Fois, R. Seraglia, G. Tabacchi, M. Roverso, G. Pagot, C. Invernizzi, A. Gasparotto, A. A. Heidecker, A. Pöthig, E. Callone, S. Dirè, S. Bogialli, V. Di Noto and C. Maccato, *Dalton Trans.*, 2023, **52**, 10677–10688.
67 C. Invernizzi, G. Tabacchi, R. Seraglia, M. Benedet, M. Roverso, C. Maccato, S. Bogialli, D. Barreca and E. Fois, *Molecules*, 2024, **29**, 642.
68 T. Shinagawa, A. T. Garcia-Esparza and K. Takanabe, *Sci. Rep.*, 2015, **5**, 13801.
69 A. Kundu, S. Gautam and B. Chakraborty, *J. Mater. Chem. A*, 2025, **13**, 2920–2933.
70 S. L. Dudarev, G. A. Botton, S. Y. Savrasov, C. J. Humphreys and A. P. Sutton, *Phys. Rev. B: Condens. Matter Mater. Phys.*, 1998, **57**, 1505–1509.
71 E. Fois, C. Maccato, D. Barreca, C. Invernizzi and G. Tabacchi, *Dalton Trans.*, 2025, **54**, 2765–2775.
72 D. Vanderbilt, *Phys. Rev. B: Condens. Matter Mater. Phys.*, 1990, **41**, 7892–7895.
73 K. F. Garrity, J. W. Bennett, K. M. Rabe and D. Vanderbilt, *Comput. Mater. Sci.*, 2014, **81**, 446–452.
74 J. P. Perdew, K. Burke and M. Ernzerhof, *Phys. Rev. Lett.*, 1996, **77**, 3865–3868.
75 E. Fois and G. Tabacchi, *Small Struct.*, 2025, **6**, 2400346.
76 S. Grimme, S. Ehrlich and L. Goerigk, *J. Comput. Chem.*, 2011, **32**, 1456–1465.
77 M. Cococcioni and S. de Gironcoli, *Phys. Rev. B: Condens. Matter Mater. Phys.*, 2005, **71**, 035105.
78 L. Bigiani, T. Andreu, C. Maccato, E. Fois, A. Gasparotto, C. Sada, G. Tabacchi, D. Krishnan, J. Verbeeck, J. R. Morante and D. Barreca, *J. Mater. Chem. A*, 2020, **8**, 16902–16907.
79 L. Bigiani, D. Zappa, D. Barreca, A. Gasparotto, C. Sada, G. Tabacchi, E. Fois, E. Comini and C. Maccato, *ACS Appl. Mater. Interfaces*, 2019, **11**, 23692–23700.
80 M. Kawamura, Y. Gohda and S. Tsuneyuki, *Phys. Rev. B: Condens. Matter Mater. Phys.*, 2014, **89**, 094515.
81 P. E. Blöchl, O. Jepsen and O. K. Andersen, *Phys. Rev. B: Condens. Matter Mater. Phys.*, 1994, **49**, 16223–16233.